Astronomy & Astrophysics manuscript no. output
May 28, 2021

No swan song for Sun-as-a-star helioseismology: performances of Solar-SONG for individual mode characterisation

S.N. Breton[1], P.L. Pallé[2,3], R.A. García[1], M. Fredslund Andersen[4], F. Grundahl[4], J. Christensen-Dalsgaard[4], H. Kjeldsen[4], and S. Mathur[2,3]

[1] AIM, CEA, CNRS, Université Paris-Saclay, Université de Paris, Sorbonne Paris Cité, F-91191 Gif-sur-Yvette, France
e-mail: sylvain.breton@cea.fr
[2] Instituto de Astrofísica de Canarias, 38205 La Laguna, Tenerife, Spain
[3] Departamento de Astrofísica, Universidad de La Laguna (ULL), 38206 La Laguna, Tenerife, Spain
[4] Stellar Astrophysics Centre, Aarhus University, 8000 Aarhus C, Denmark

ABSTRACT

The GOLF instrument has flown aboard SoHO for almost 25 years but aging of the instrument has now strongly affected its performance, especially in the low-frequency p-mode region. SoHO's situation is nominal and, except for the SoHO 1998 vacation weeks, GOLF has been working since 11th April 1996 without severe incident in its third operating mode (the first two operating modes are not available anymore due to damage in the optical system motorisation). However, after such a long time of flight, the SoHO mission will finally end at some point and the ground-based network BiSON will remain the only facility able to perform Sun-integrated helioseismic observations. It is therefore time to prepare the future of spectroscopic helioseismic observations. We want to assess the helioseismic performances of an échelle spectrograph like SONG. Indeed, the high precision of such an instrument and the quality of data acquired for asteroseisismic purpose encourage us to go deeper into the possibility offered to probe the solar interior. Because of the limitations of single-site ground-based observations and the short duration of the available time series making it difficult to do direct analysis of lower frequency regions, we decide to focus on the analysis of the detection quality of mid- and low-frequency p modes. We use the data acquired during the Solar-SONG 2018 observation campaign at the Teide Observatory. Solar-SONG data are reduced with the combination of the traditional IDL `iSONG` pipeline and a new `Python` pipeline described in this paper. A peakbagging process built around a Bayesian approach is then performed on the Solar-SONG and contemporaneous GOLF one-month long spectrum. The aging of GOLF is evaluated through the evolution of its p-mode low-frequency detection quality over the years. We are able to fit precise parameters for p modes at a lower frequency for Solar-SONG data than for the contemporaneous GOLF data. Indeed, the first mode is fitted for Solar-SONG at ≈ 1750 μHz against ≈ 2157 μHz for GOLF. We also observe that the noise level in the Solar-SONG 1 to 1.5 mHz region is lower than any considered GOLF subseries.

Key words. Methods: data analysis – Sun: helioseismology

1. Introduction

The first detection of oscillations in the Sun (Leighton et al. 1962; Noyes & Leighton 1963) was possibly the event that changed forever the flow of solar and stellar physics, by opening a totally new horizon for stellar interior dynamics studies. A few years later, Ulrich (1970) and Leibacher & Stein (1971) linked those oscillations to a global resonant phenomenon. Christensen-Dalsgaard & Gough (1976), commenting on the identification of high-degree modal structure in the observed five-minute oscillations (Deubner 1975) and the claimed detections of the 160 minute g mode by Brookes et al. (1976) and Severnyi et al. (1976) and claimed oscillations in the solar diameter (Hill & Stebbins 1975), underlined that such observations would open the way to obtain precise inference about the deep interior of the Sun. Sun-as-a-star observations of low-degree p modes by Claverie et al. (1979) really set the start of the helioseismic era. Microvariability and Oscillations of STars (MOST, Matthews et al. 2000), Convection, Rotation and planetary Transit (CoRoT, Auvergne et al. 2009), *Kepler*/K2 (Borucki et al. 2011; Howell et al. 2014) and Transiting Exoplanet Survey Satellite (TESS, Ricker et al. 2015) space missions drove the discipline towards new stars and new horizons. Indeed, over the past two decades, asteroseismology has fruitfully probed the deep layers of what constitutes now a tremendous amount of stars (e.g. García & Ballot 2019). Just considering solar-like oscillations, it has been made possible to evaluate the core rotation rate of red giants (Beck et al. 2011; Bedding et al. 2011; Mosser et al. 2011) and the outcome brought by these analyses disrupted the landscape of what was commonly accepted in stellar evolution models concerning angular momentum transport. Combined with previous results obtained with solar data, these observations have been puzzling the mind of theoreticians over the last decade (see e.g. Mathis 2013; Aerts et al. 2019, and references therein). One of the keys of the enigma resides in the deep-interior dynamics of main-sequence stars and will be obtained only through the detection of individual gravity modes (further denoted g modes) in low-mass stars. Since the first days of helioseismology, the Sun has always remained the most obvious candidate to observe g modes in a main-sequence star with solar-like pulsations (Appourchaux & Pallé 2013). Indeed, the fact that we are now able to probe the core dynamics of stars located hundreds of light years away from the Earth while being kept in the dark concerning our own star is somehow incredibly frustrating.

Important means were deployed in order to acquire well-resolved, high-standard spectra of solar oscillations. From 1976,

Mark-I, the first node of what would become the Birmingham Solar Oscillations Network (BiSON, Chaplin et al. 1996) was deployed in Tenerife at the Teide Observatory. The IRIS network (Salabert et al. 2003) operated from 1989 to 1999 while the Global Oscillations Network Group (GONG, Harvey et al. 1996) began operating in 1996. However, the culminating event of the golden era of helioseismology was without doubt the launch of the Solar Heliospheric Observatory (SoHO, Domingo et al. 1995). Bringing to space three instruments dedicated to probe the solar interior, SoHO was thought to embark all the tools needed to unravel the last mysteries hidden by the core of our star.

Taken aboard SoHO, the Global Oscillations at Low Frequency (GOLF, Gabriel et al. 1995) instrument was expected to be the one that would bring for the first time an unambiguous detection of g modes. With its sodium cell and its two photomultipliers, GOLF was designed to perform differential intensity measurements over both wings of the sodium solar doublet. Those intensity measurements could then be exploited to obtain an extremely precise radial-velocity (RV) measurement of the upper layers of the Sun. Over the years, several individual g-mode candidates were reported (Gabriel et al. 2002; Turck-Chièze et al. 2004; García et al. 2011) while a global g-mode pattern was identified with a 99.49 % confidence level (García et al. 2007). More recent claims of g-mode detection with GOLF (Fossat et al. 2017) are still under discussion (Schunker et al. 2018; Appourchaux & Corbard 2019; Scherrer & Gough 2019).

The Stellar Observations Network Group initiative (SONG, Grundahl et al. 2007) was conceived with the goal to install an asteroseismology dedicated terrestrial network with several operating nodes in order to maximise the observational window. Stellar observations are performed by a robotised telescope, the light being driven onto a high-resolution échelle spectrograph. The acquired spectra are then reduced to obtain high-precision radial-velocity measurements. The prototype and first node, equipped with the one-meter Hertzsprung telescope, was built at the Teide Observatory and began its operation in 2014 (Andersen et al. 2016). In June 2012, as the installation of the telescope was delayed, the spectrograph was plugged on an optical fibre mounted on a solar tracker in order to collect solar light during the day (Pallé et al. 2013). This operation represented the first light of the Solar-SONG initiative. This was the first time a multi-wavelength spectrograph was used to collect direct solar observations with a helioseismology-dedicated purpose. Such an approach is thought to exploit the fact that the convective noise is expected to be partially decorrelated at different wavelengths while the p-mode signal remains coherent, as it was highlighted in the past by a short testing run with the GOLF-NG prototype (Turck-Chièze et al. 2008; Salabert et al. 2009). Independently from the Solar-SONG initiative, Sun-as-a-star observations were performed with the spectrograph HARPS-N (Dumusque et al. 2015). The purpose of this study was to increase RV measurements precision by improving the characterisation of stellar noise in the signal, with the objective to enable the detection of Earth-twins around solar-like stars (with a long cadence not well suited for p-mode observation).

The power spectrum of one week of Solar-SONG observation was compared with GOLF and Mark-I contemporaneous spectra and it could be shown that the power in high-frequency regions (dominated by photon noise) was 2.5 and 4.4 times lower than in Mark-I and GOLF, respectively. A daily synoptic follow-up of the Sun has been realised since 2017. During the summer 2018, a high-cadence campaign was carried out in order to evaluate the helioseismical performance of the instrument. First results of this campaign were presented in Fredslund Andersen et al. (2019b).

A first perspective of the promises offered by an échelle spectrograph like Solar-SONG to explore the low-frequency regions of the solar power spectrum may be obtained by considering the instrument's ability to detect low-frequency p modes during the high-cadence campaign. The purpose of this work is therefore to complete and extend the previous analyses by assessing Solar-SONG performances in mid- and low-frequency p-mode regions. GOLF appears as a natural reference to evaluate the Solar-SONG abilities.

The layout of the paper is as follows. Section 2 presents the solar time series that were used for this work. We also give some details about the Solar-SONG data reduction method. In Sect. 3, the peakbagging process that was applied on the power spectrum density (PSD) obtained from the time series is described. We use the peakbagging results to compare GOLF and Solar-SONG performances in Sect. 4. Those results and the perspectives opened by the promising performance of Solar-SONG are discussed in Sec. 5.

2. Data acquisition and reduction

The Solar-SONG high-cadence observation campaign was performed from May 27 to July 22, 2018. Observations were carried out in a fully automatic way and the scheduling was handled by the automation software "the Conductor" (Fredslund Andersen et al. 2019a). In this work, we consider only thirty days of observation, from June 3 to July 2. The reason of this choice is that this interval of time represents the best set of consecutive days with a satisfactory duty cycle of 47%. These observations yield an acceptable balance between resolution and windowing effects caused by the duty cycle.

2.1. GOLF data reduction

Due to a loss in photomultiplication rate, GOLF mean noise level has been increasing over the years (García et al. 2005; Appourchaux et al. 2018) in high and medium frequency regions. Above 4 mHz and around 1 mHz, the photon noise power contribution dominates the PSD. Not only do we want to compare Solar-SONG performances to what GOLF is now, but also to what it used to be. We therefore select 22 time series of same length, all at similar epoch of the year in order to ensure that SoHO position on its orbit is each time comparable to what it was during the summer 2018.

GOLF time series used in this work are calibrated using the method described in García et al. (2005). GOLF measurements are obtained using the instrument's own time reference and not the SoHO main on-board time reference. However, during SoHO's operations, the GOLF clock experienced on several occasions unexpected events that resulted in time lags (Appourchaux et al. 2018). The Variability of solar IRradiance and Gravity Oscillations instrument (VIRGO, Fröhlich et al. 1995), also embarked on SoHO but synchronised on SoHO main on-board time, has been used as a reference to cross-correlate GOLF measurements and correct any timing issue on GOLF.

2.2. Solar-SONG data reduction

In high-cadence mode, the SONG spectrograph acquires a spectrum approximately every 3.5 seconds, with an exposure time below one second. The acquired spectrum covers a range from

4400 to 6900 Å, with a pixel scale of 0.022 Å. A spectrum is divided into 51 orders. However, solar observations have been obtained with the spectrograph iodine cell, and for those observations, only 24 orders are used (from 4994 to 6208 Å). The IDL `iSONG` (Corsaro et al. 2012; Antoci et al. 2013) pipeline has been designed to reduce those spectra and provide RV measurements. The method that has been developed over the last decades consists in dividing each order of the spectrum into so-called *chunks* and to compute an RV for each of those chunks (see e.g. Butler et al. 1996). 22 chunks per order are used for Solar-SONG spectra. For each spectrum, `iSONG` produces data outputs denoted as *cubes*. These cubes are built as 22x24x27 arrays: 27 tags are linked to each chunk, among which the identifiers of the chunk (given by the order number and the rank of the chunk among the order), the computed RV, the photon flux level, and the observation time.

The `iSONG` pipeline is able to carry out the data processing and produces an integrated RV over the chunks, but we introduce in this paper a complementary `Python` framework dedicated to obtain this integrated RV starting from the `iSONG` cubes. This reduction framework is packaged as the `songlib` submodule of the `apollinaire`[1] library (see Breton et al. in prep and appendix B). In particular, this framework has been designed to reduce data (originally unequally sampled with one spectrum acquired every $\sim$ 3.5 s) into regularly sampled velocity measurements. For this work, we produced data sampled at 20 seconds.

Corrections are performed day by day. The first step is to integrate the chunk-relative RV to get a one-dimensional RV vector. Weights are attributed to each chunk by considering

$$w_{ij} = \frac{1}{\sigma_{ij}^2} \, , \tag{1}$$

where σ_{ij} is the robust standard deviation of the non-zero RV measurements of the j^{th} chunk of the i^{th} order. The robust standard deviation σ is computed as follows from the median absolute deviation, MAD:

$$\sigma \approx \frac{\text{MAD}}{\Phi^{-1}(3/4)} \approx 1.4826 \, \text{MAD} \, , \tag{2}$$

where Φ^{-1} is the normal inverse cumulative distribution function evaluated at probability 3/4. If $\sigma_{ij} > 1$ km/s or $\sigma_{ij} < 3$ m/s, the corresponding weight is set to 0. We check that we obtain the same results with `songlib` and `iSONG`. Using the σ_{ij}, the one-dimensional RV vector is computed as the weighted average of the 528 RV vectors. Considering the rms of the point-to-point difference of these daily time series, we compute a proxy u for the spectrograph single-point precision. The proxy is taken as the mean of the obtained rms values

$$u = \frac{1}{\sqrt{2}} \overline{\underset{i}{\text{rms}}} \, (v_{i+1} - v_i) \, , \tag{3}$$

where v_i and v_{i+1} are consecutive RV measurements; we get 0.88 ± 0.13 m.s^{-1}

The second step is to correct and re-sample this vector. In order to have RV measurements regularly sampled, so-called *boxes* of 20 seconds are computed and each cube is attributed to a box. The timestamps of the boxes are computed considering the center of the box. For each of those boxes, the mean RV is computed and measurements lying beyond three standard deviations are removed. The same process is repeated with the remaining measurements, this time considering a two-standard-deviation threshold. Some outliers are again removed by considering means over a neighborhood of 50 boxes (1000 seconds) and getting rid of measurements outside of eight standard deviations the first time, six standard deviations the second time. The RV inside each box is computed as the mean of the remaining cubes values.

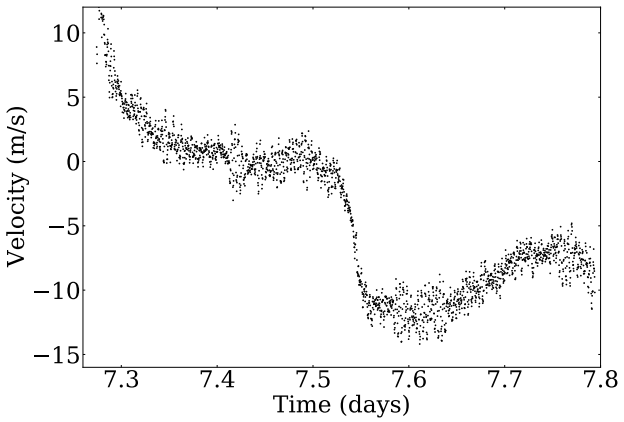

Fig. 1. Residual trend remaining before application of the FIR filter in the seventh day of the considered Solar-SONG time series (10 July 2018).

The ephemeris velocity[2] with barycentric correction is finally substracted from each box measurement. The Julian time noon value is also substracted from every measurement so that the residual trend after the ephemeris correction is centered around zero velocity (see Fig. 1).

The last step consists in high-pass filtering and final corrections. During the observation campaign, the alto-azimuthal solar tracker was set to follow a pre-computed solar ephemeris without any servo correction. This effect introduces daily low-frequency trends in the RV measurements, especially around the solar meridian crossing. To get rid of the terrestrial rotation harmonics that this would generate in the spectrum, we filter out every frequency below 800 μHz with a finite impulse response (FIR) filter. The transfer function of the FIR filter is represented in Fig. 2. The time series have been extensively visually inspected and time intervals with inconsistent RV measurements are set to zero at this stage[3]. Considering the mean photon flux level, measurements below a threshold of 12,000 ADU are also set to zero. Considering non-zero RV mean values over the full day, values beyond respectively 3.5 and 3 standard deviations are removed during two final cleaning operations.

Fig. 3 shows GOLF and Solar-SONG time series and corresponding PSD. We also provide an insight at the [1500-2500 μHz] and [4000-5000 μHz] regions of the PSD in Fig 4. The time series have been restricted to one hour and a half in Fig. 5 in order to highlight the presence of the five-minute oscillation in the signal. Figure 6 presents the same panels as in Fig. 3 but with the observational window of Solar-SONG data applied on GOLF time series. Due to the convolution by the observational window, the power of the p-mode peaks is redistributed within

[1] The source code is available at `https://gitlab.com/sybreton/apollinaire`

[2] `https://ssp.imcce.fr/forms/visibility`

[3] The exhaustive list of corrections can be found at: `https://gitlab.com/sybreton/apollinaire/-/blob/master/apollinaire/songlib/interval_nan.py`

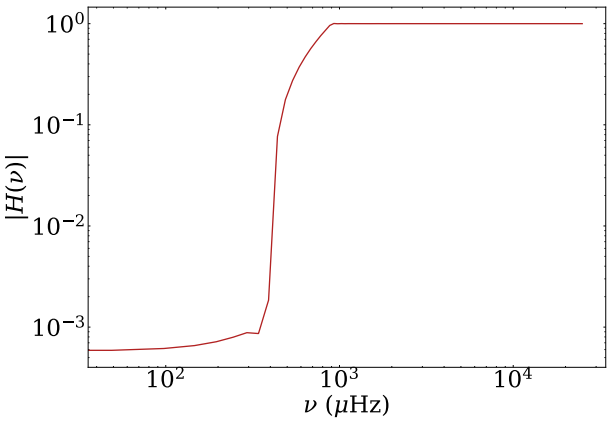

Fig. 2. Modulus of the transfer function H of the FIR filter applied on the Solar-SONG time series.

sidelobe peaks. The 800 μHz cut of the Solar-SONG time series FIR filter is visible. It also appears clearly on the PSD visual comparison that the Solar-SONG mean noise level around the p-mode bump is lower for Solar-SONG, at low and high frequency. The GOLF excess of power in high-frequency p modes is explained by the chromospheric contribution to the sodium solar line profile (Jiménez-Reyes et al. 2007).

3. Peakbagging process

The PSD follows a χ^2 law with two degrees of freedom (Woodard 1984). Assuming that frequency bins are independent from each other, the relevant likelihood is given by:

$$\mathcal{L}(\mathbf{S_x}, \theta) = \prod_{i=1}^{k} \frac{1}{S(\nu_i, \theta)} \exp\left[-\frac{S_{x_i}}{S(\nu_i, \theta)}\right] , \quad (4)$$

where S denotes the ideal spectrum parametrised by a set θ of parameters. S is considered against the observed spectrum $\mathbf{S_x}$ at a given set of k frequency bins ν_i.

Fits are processed using a Bayesian approach. Monte Carlo Markov Chains (MCMC, Sokal 1997; Liu 2009; Goodman & Weare 2010) are used to evaluate the shape of the posterior probability distribution of our model:

$$p(\theta|\mathbf{S_x}) = \frac{p(\mathbf{S_x}|\theta)p(\theta)}{p(\mathbf{S_x})} , \quad (5)$$

where $p(\mathbf{S_x}|\theta)$ is the likelihood $\mathcal{L}(\mathbf{S_x}, \theta)$, $p(\theta)$ the prior probability and $p(\mathbf{S_x})$ a normalisation factor. In practice, only the numerator $p(\mathbf{S_x}|\theta)p(\theta)$ of the posterior probability distribution is sampled by the MCMC. In this work, all priors $p(\theta)$ have been taken as uniform distributions.

MCMC are sampled with the `emcee`[4] (Foreman-Mackey 2016) implementation through the `apollinaire`[5] (Breton et al. in prep) peakbagging library. In this work, MCMC have been sampled considering 500 walkers and 2000 iterations, with the 200 first iterations being discarded as burned-in. Consequently, each sampled MCMC is constituted of 900,000 points after the discarding step. The uncertainties σ_+ and σ_- over each parameter are computed considering the 16th and 84th centiles of the sampled distribution (which approximates the standard deviation in case of a Gaussian distribution).

Our fitting strategy is the following: first, a global background model is adjusted to the PSD. In the second step, the PSD is divided by this background model to obtain a spectrum with a signal-to-noise magnitude (the so-called *signal-to-noise spectrum*) that we use to fit the p modes. Modes are fitted by odd pair $\ell = \{1, 3\}$ and even pair $\ell = \{0, 2\}$ assuming a Lorentzian profile. Due to the low resolution of the spectrum, we do not add splittings or asymmetries to our model. The height H and width Γ are set to vary freely for each mode.

The background for the GOLF spectrum is fitted considering the sum of one Harvey profile (Harvey 1985) and the high frequency noise. As Solar-SONG time series have been filtered with a 800-μHz high pass filters, we do not fit any background on the spectrum and, in order to get the signal-to-noise spectrum, we only divide the PSD by the mean value of the high frequency noise (above 8 mHz).

In this work, each fitted MCMC has been inspected through its cornerplot representation and fits which do not learn anything from the priors have been rejected (that is fits for which the marginalisation over each parameter of the sampled posterior probability distribution still has a uniform distribution shape). After this first step, for each fitted mode, we computed a proxy of the natural logarithm of the Bayes factor $\ln K$ (Kass & Raftery 1995; Davies et al. 2016), related to the rejection of the null hypothesis H0. We thinned the MCMC from 900,000 to 9,000 sets of parameter in order to save some computing time when computing $\ln K$ (more details on the way $\ln K$ is computed by `apollinaire` are given in Breton et al. in prep). We remind here the interpretation of the $\ln K$ value:

$$\ln K = \begin{cases} < 0 & \text{favours H0} \\ 0 \text{ to } 1 & \text{not worth more than a bare mention} \\ 1 \text{ to } 3 & \text{positive} \\ 3 \text{ to } 5 & \text{strong} \\ > 5 & \text{very strong} \end{cases}$$

3.1. Dealing with observational windows

Solar-SONG is a single site ground-based instrument. The duty cycle of the observations is thus conditioned by the day-night cycle. According to the Fourier theorem, the consequence of the gaps in the time series is the convolution of the PSD by a sinc function (e.g. Salabert et al. 2002, 2004; García 2015). Therefore the statistics of the PSD is no longer a χ^2 with two degrees of freedom, as frequency bins are no longer independent from each other. However, the correct likelihood (Gabriel 1994) is excessively complex and its implementation is beyond the scope of this paper. We therefore decide to ignore this issue and to fit all our data, even the windowed one, considering the χ^2 likelihood presented in equation 4.

In order to overcome the issue of the mode profile modification due to the convolution, we use an *ad hoc* correction to our model. First, we define the observational window vector as a boolean vector of the same length as the actual time series. Considering a given time stamp, the value of the observational window vector is 1 if the RV value at this time stamp is non-zero, 0 otherwise. The Fourier transform of the observational window vector is then computed (see Fig. 7). The heights and the frequencies of the peaks above a certain threshold (10% of the height of the zero-frequency peak) are stored and will be used to build the sidelobe structure of each considered mode. The com-

[4] `https://emcee.readthedocs.io/en/stable`
[5] `https://apollinaire.readthedocs.io/en/latest`

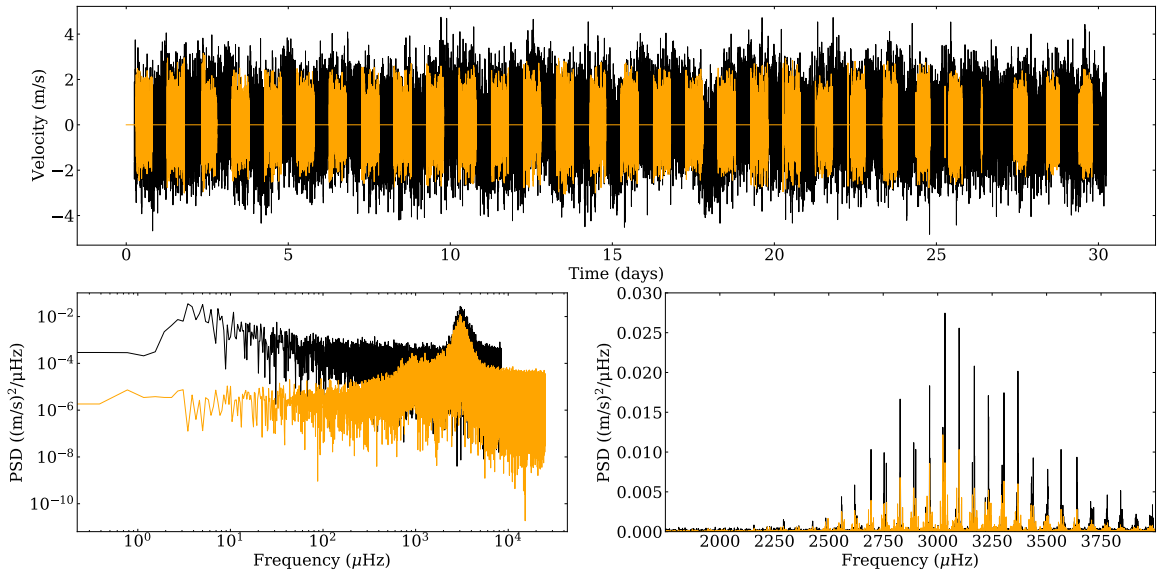

Fig. 3. *Top panel:* Solar-SONG (orange) and GOLF (black) complete time series from 3 June to 2 July 2018. *Bottom left:* corresponding PSD. *Bottom right:* Zoom into the p-mode region.

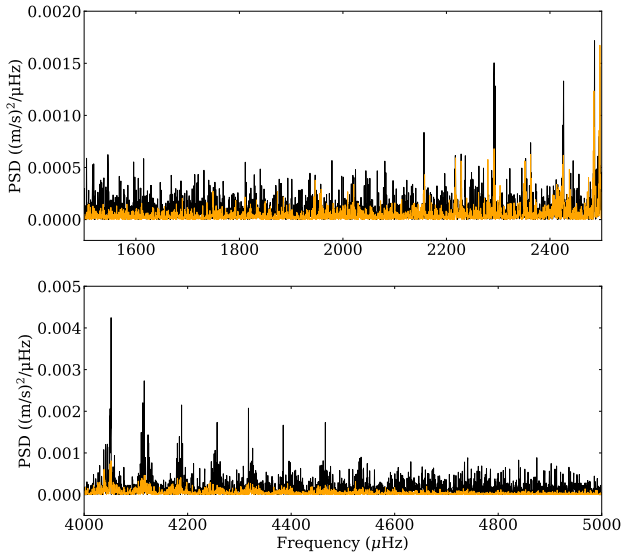

Fig. 4. GOLF (black) and Solar-SONG PSD in the [1500-2500 μHz] (*top*) and [4000-5000 μHz] (*bottom*) regions.

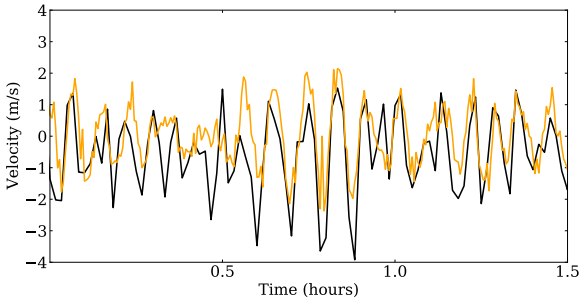

Fig. 5. One hour and a half of the Solar-SONG (orange) and GOLF (black) RV time series. The Solar-SONG time series is sampled at 20s and the GOLF time series is sampled at 60s.

parison of the structure of the $n = 21$ even pair in GOLF data, with and without the Solar-SONG-like observational window, is represented in Fig. 8. The method presented above enables to accurately model the mode profile when the observational window has daily gaps. It is also interesting to note that one of the $\ell = 0$ sidelobe power excesses lies very close to the $\ell = 2$ central frequency, and reciprocally for one of the $\ell = 2$ sidelobes.

4. Solar-SONG compared to GOLF

Considering the contemporaneous series, we are able to fit modes in Solar-SONG spectrum at lower frequencies than in GOLF (even when considering the GOLF time series with full duty cycle). Indeed, the first well-fitted Solar-SONG mode is $n = 11$, $\ell = 1$ at 1749.67 ± 1.36 μHz, while for GOLF it is $n = 14$, $\ell = 1$ at 2156.57 ± 0.86 μHz. All the fitted frequencies can be visualised thanks to the échelle diagrams (see Fig. 9). The power excess of the sidelobes of the $\ell = 0$ and $\ell = 1$ modes appear clearly in the middle and bottom panel. It should be stressed that several $\ell = 3$ frequencies could not be fitted when applying the Solar-SONG-like window on GOLF, although those modes have been successfully fitted in the real GOLF spectrum and in the Solar-SONG spectrum. The variation of mode heights and widths with frequency can be found in Fig. 10 and Fig. 11. It is not surprising that the height of the modes fitted with Solar-SONG are smaller than for GOLF: for each mode, the sidelobe power redistribution is considered relatively to the height of the central mode and it is the actual height of this central peak in the

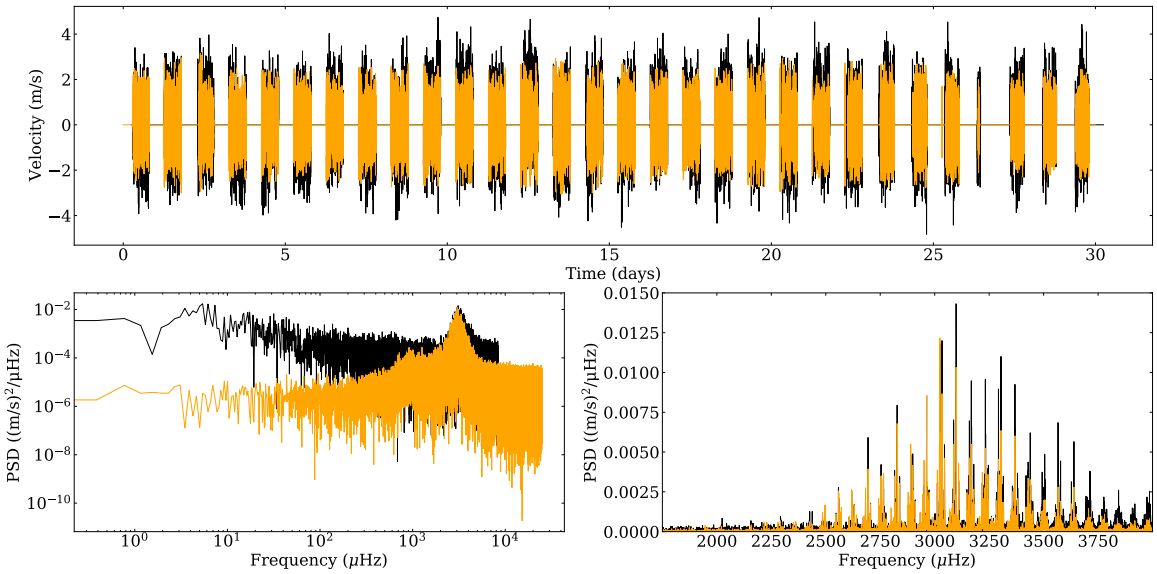

Fig. 6. Same as Fig. 3 but with an observational window similar to the one of Solar-SONG applied on GOLF time series.

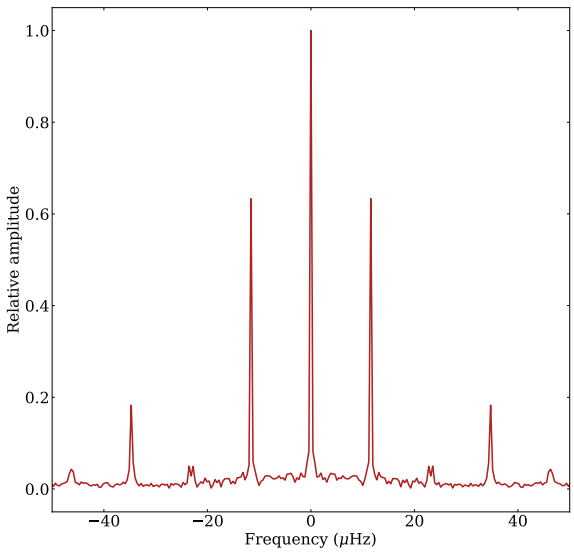

Fig. 7. Modulus of the Fourier transform of Solar-SONG observational window. The amplitude is normalised to the height of the zero-frequency peak.

spectrum that is represented in the figure. At high frequency, as it was already visible in Fig. 6, the height of the modes observed by GOLF are larger due to the chromospheric contribution to the solar sodium doublet. Widths are in good agreement between the three fitted spectra, except for $\ell = 1$ modes, where Solar-SONG observed widths seem systematically overestimated below 3 mHz.

Another interesting aspect of the comparison between the two instruments is the inability of the code to fit the $n = 16$, $\ell = 0$ mode in the GOLF spectrum while this same mode is well characterized for Solar-SONG. It seems that during the time of observation, this mode was much less excited than its $\ell = 0$ neighbours. Visually inspecting the GOLF spectrum, it appears that the mode structure is quite difficult to distinguish from the surrounding noise, while the SNR appears to be much higher in the Solar-SONG spectrum. That is due to the different spatial sensibility of GOLF in its single-wing configuration (García et al. 1998).

The full set of parameters of the modes fitted for each spectrum can be found in Table A.1, A.2 and A.3. For each mode, the $\ln K$ value is also provided. Note that the minimal uncertainties over frequencies are typically close to the spectrum resolution ($\approx$ 0.39 μHz).

4.1. Evaluating GOLF aging over the years

Considering the integrated power in the 1000-1500 μHz region of the GOLF spectrum, Appourchaux et al. (2018) exhibited evidence of the increase of low-frequency noise (which is a combination of photon noise and solar convective noise) in the data over more than two decades of solar observations. This increase is related to the aging of the two photomultipliers, the entrance window, and the interference filter of the instrument, as it was already underlined by García et al. (2005) when they analysed the increase of instrumental photon noise of the instrument from 1996 to 2004. It is straightforward to check that, considering the 2018 observing campaign, the mean power value in the 1000-1500 μHz region is an indicator largely in favour of Solar-SONG: this value is 29.1 $m^2s^{-2}Hz^{-1}$ against 104 $m^2s^{-2}Hz^{-1}$ for GOLF. We note that the same comparison in the 5000-6000 μHz region yields 14 $m^2s^{-2}Hz^{-1}$ for Solar-SONG and 103 $m^2s^{-2}Hz^{-1}$ for GOLF.

Actually, running this analysis over each 30-day GOLF series we consider in this work (see Fig. 12) unveils evidence that the Solar-SONG noise level in this region, is comparable, if not smaller, to what it was for GOLF in the best years of the in-

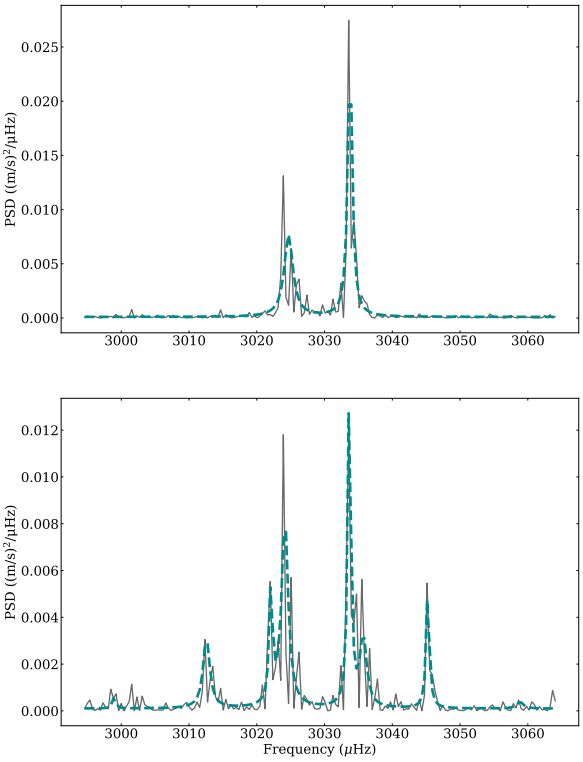

Fig. 8. Mode profile of the GOLF mode $n = 21$ even pair, with real duty cycle (*top*) and considering a Solar-SONG like window (*bottom*). The results of the fit is plotted in dashed cyan over the data in grey.

strument. The power decrease observed from 1996 to 1999 can probably be linked to the minimum of magnetic activity reached at this time. After this date, ignoring some yearly modulations, the mean power level in this frequency region increases continually.

The second step of this GOLF yearly evolution analysis is to consider the mode orders for which, considering the 2018 GOLF series, we were not able to provide mode parameters although some of those modes were fitted considering Solar-SONG data. With Solar-SONG, we were able to fit the $n = 11$, $\ell = 1$ mode while for GOLF we had to stop at the $n = 14$, $\ell = 1$ mode. We therefore decide to perform our peakbagging process for odd and even pairs of order 11 to 14 on each GOLF 30-day series. The results are summarised order by order and degree by degree in Fig. 13. The mode frequency variations are related to the magnetic solar activity (Woodard & Noyes 1985; Palle et al. 1989). Modes that are not represented in this figure could not be fitted or the uncertainty on fitted frequency was above 2 μHz. The $n = 11$, $\ell = 1$ could not be fitted in the considered GOLF series after 2005. For this order, we were not able to fit any $\ell = 2$ or $\ell = 3$ modes. The only mode we were able to fit almost every time until 2018 is the $n = 14$, $\ell = 1$. It should be reminded that for such short time series, our ability to fit a given mode is not only dependent to the instrumental SNR ratio but also to the excitation state of the mode. This explains why for certain series, some modes could not be fitted although GOLF instrumental noise did not increase drastically or was even smaller.

5. Discussion

The promising helioseismic measurements deserve to be refined with longer observations with better duty-cycle. This second condition can only be achieved if other SONG nodes are able to perform solar high-cadence observations. Presently (2021), a new node of the SONG network is being commissioned at the Mt. Kent Observatory in Queensland, Australia. The spectrograph there is purely fibre-fed and is 'readied' for solar observations - although, at present, a solar tracker, nor fibres to feed the light to the spectrograph have been installed. Installing such a system would obviously allow a significant improvement to the duty-cycle of solar observations. Reducing the effects of the sidelobes, high duty-cycle observations campaign would allow enforcing the statistical robustness of the peakbagging analysis we performed in this work. It would sensibly minimise the blurring effect between $\ell = 0$ and $\ell = 2$ modes that we presented in Fig. 8.

In order to go deeper into the low-frequency study of the Solar-SONG spectrum, the solar-tracker used for the 2018 observation campaign should also be modified. The current Solar-SONG set-up uses an azimuthal commercial mount which is not optimal for stability in spectral regions below 800 μHz. Indeed, the daily Earth-motion RV residual that appears in Fig. 1 creates a high- amplitude harmonic pattern in the PSD if the low-frequency trends of time series have not been properly filtered out with the FIR filter. It should be noted that the servo guidance was not active during the 2018 campaign unlike what was planned and the solar tracker followed the Sun motion using only pre-computed ephemeris. However we noticed during a short test run performed in 2019 that turning on the servo introduced additional low-frequency trends in the RV signal. To overcame this limitation and also to provide continuity and more scientific capabilities to the current Solar-SONG initiative (helioseismology and synoptics solar program), a new project was submitted and recently properly funded, named Magnetrometry Unit for SOLar-SONG (MUSOL) which includes not only a proper equatorial robust mount with precise guiding ($\sim$ 1 arcsec rms) but also a new polarimetric unit attached to the mount with the modulation unit and fibre optics to feed the SONG spectrograph. Its main scientific objective will be to measure the magnetism of the global Sun (both vectors components of the magnetic field). The dipolar and quadrupolar components of the global magnetic field can only be measured by detecting the weak polarization signals induced by the Hanle effect in some spectral lines. A long term and continuous solar observations with this new polarimetry could in principle be sensitive enough to measure the dipole component of the global solar magnetic field and its variation along the solar activity cycle (see Vieu et al. 2017).

6. Conclusion

In this work, we presented a new reduction pipeline for Solar-SONG data. We compared the contemporaneous GOLF and Solar-SONG observations by performing a peakbagging analysis with a Bayesian approach. On the one hand, by studying the PSD of the Solar-SONG data, we were able to identify structures at lower frequency than in the GOLF PSD. On the other hand, we evaluated the aging of GOLF by considering the yearly mean power evolution in the 1 to 1.5 mHz region in 30-days

long series. For each considered series, the mean power level was above the mean power level obtained in 2018 with Solar-SONG. We then performed another peakbagging analysis on those series focusing on the low-frequency modes for which we were able to provide mode parameters for Solar-SONG and not for GOLF in the 2018 comparison. We were able to provide good frequency estimates for many of those modes in the first years of SoHO's operation; however, around 2005, the noise level increase in those frequency regions allowed us to fit only the $\ell = 1$ modes with sufficient SNR.

Nevertheless, despite its aging, GOLF remains an invaluable asset for helioseismology. Indeed, it has been almost continuously collecting data over the last 25 years and will carry on in its mission in the years to come. However, the present analysis suggests that échelle spectrographs may embody the future of both helioseismology and asteroseismology. Indeed, coupled with its telescope and its solar tracker, the Teide SONG node is theoretically able to perform observations day and night. The real-time reduction of high-cadence solar measurements represents a challenge that is currently undertaken by the development of dedicated IDL and `Python` pipelines.

Acknowledgements. This work is based on observations made at the Hertzsprung SONG telescope operated at the Spanish Observatorio del Teide on the island of Tenerife by the Aarhus and Copenhagen Universities and by the Instituto de Astrofísica de Canarias. S.N.B. and R.A.G acknowledge the support from PLATO and GOLF CNES grants. Funding for Solar-SONG was provided by the Excellence 'Severo Ochoa' programme at the IAC and the Ministry MINECO under the program AYA-2016-76378-P. Funding for the Stellar Astrophysics Centre is provided by The Danish National Research Foundation (Grant DNRF106). We would like to acknowledge the contribution of the engineers at the IAC, Felix Gracia (optical), Ezequiel Ballesteros (electronics) and the support from the day-time operator at the SolarLab, Teide Observatory, on this Solar-SONG initiative and during the campaign. We thank Dr. Kun Wang (China West Normal University) for his dedicated effort during the campaign with data handling and analysis of the observations. The solar visibility calculations were carried out by the ephemeris calculation service of the IMCCE through its Solar System portal (`https://ssp.imcce.fr`).

Software: `Python` (Van Rossum & Drake 2009), `numpy` (Oliphant 2006; Harris et al. 2020), `pandas` (pandas development team 2020; Wes McKinney 2010), `matplotlib` (Hunter 2007), `emcee` (Foreman-Mackey et al. 2013), `scipy` (Virtanen et al. 2020), `corner` (Foreman-Mackey 2016), `astropy` (Astropy Collaboration et al. 2013, 2018).

The source code used to obtain the present results can be found at `gitlab.com/sybreton/apollinaire`.

References

Aerts, C., Mathis, S., & Rogers, T. M. 2019, ARA&A, 57, 35
Andersen, M. F., Grundahl, F., Beck, A. H., & Pallé, P. 2016, in Revista Mexicana de Astronomia y Astrofisica Conference Series, Vol. 48, Revista Mexicana de Astronomia y Astrofisica Conference Series, 54–58
Antoci, V., Handler, G., Grundahl, F., et al. 2013, MNRAS, 435, 1563
Appourchaux, T., Boumier, P., Leibacher, J. W., & Corbard, T. 2018, A&A, 617, A108
Appourchaux, T. & Corbard, T. 2019, A&A, 624, A106
Appourchaux, T. & Pallé, P. L. 2013, in Astronomical Society of the Pacific Conference Series, Vol. 478, Fifty Years of Seismology of the Sun and Stars, ed. K. Jain, S. C. Tripathy, F. Hill, J. W. Leibacher, & A. A. Pevtsov, 125
Astropy Collaboration, Price-Whelan, A. M., SipHocz, B. M., et al. 2018, aj, 156, 123
Astropy Collaboration, Robitaille, T. P., Tollerud, E. J., et al. 2013, A&A, 558, A33
Auvergne, M., Bodin, P., Boisnard, L., et al. 2009, A&A, 506, 411
Beck, P. G., Bedding, T. R., Mosser, B., et al. 2011, Science, 332, 205
Bedding, T. R., Mosser, B., Huber, D., et al. 2011, Nature, 471, 608
Borucki, W. J., Koch, D. G., Basri, G., et al. 2011, ApJ, 736, 19
Brookes, J. R., Isaak, G. R., & van der Raay, H. B. 1976, Nature, 259, 92
Butler, R. P., Marcy, G. W., Williams, E., et al. 1996, PASP, 108, 500
Chaplin, W. J., Elsworth, Y., Howe, R., et al. 1996, Sol. Phys., 168, 1
Christensen-Dalsgaard, J. & Gough, D. O. 1976, Nature, 259, 89
Claverie, A., Isaak, G. R., McLeod, C. P., van der Raay, H. B., & Cortes, T. R. 1979, Nature, 282, 591
Corsaro, E., Grundahl, F., Leccia, S., et al. 2012, A&A, 537, A9
Davies, G. R., Silva Aguirre, V., Bedding, T. R., et al. 2016, MNRAS, 456, 2183
Deubner, F. L. 1975, A&A, 44, 371
Domingo, V., Fleck, B., & Poland, A. I. 1995, Sol. Phys., 162, 1
Dumusque, X., Glenday, A., Phillips, D. F., et al. 2015, ApJ, 814, L21
Foreman-Mackey, D. 2016, Journal of Open Source Software, 1, 24
Foreman-Mackey, D., Hogg, D. W., Lang, D., & Goodman, J. 2013, PASP, 125, 306
Fossat, E., Boumier, P., Corbard, T., et al. 2017, A&A, 604, A40
Fredslund Andersen, M., Handberg, R., Weiss, E., et al. 2019a, PASP, 131, 045003
Fredslund Andersen, M., Pallé, P., Jessen-Hansen, J., et al. 2019b, A&A, 623, L9
Fröhlich, C., Romero, J., Roth, H., et al. 1995, Sol. Phys., 162, 101
Gabriel, A. H., Baudin, F., Boumier, P., et al. 2002, A&A, 390, 1119
Gabriel, A. H., Grec, G., Charra, J., et al. 1995, Sol. Phys., 162, 61
Gabriel, M. 1994, A&A, 287, 685
García, R. A. 2015, in EAS Publications Series, Vol. 73-74, EAS Publications Series, 193–259
García, R. A. & Ballot, J. 2019, Living Reviews in Solar Physics, 16, 4
García, R. A., Pallé, P. L., Turck-Chièze, S., et al. 1998, ApJ, 504, L51
García, R. A., Salabert, D., Ballot, J., et al. 2011, in Journal of Physics Conference Series, Vol. 271, GONG-SoHO 24: A New Era of Seismology of the Sun and Solar-Like Stars, 012046
García, R. A., Turck-Chièze, S., Boumier, P., et al. 2005, A&A, 442, 385
García, R. A., Turck-Chièze, S., Jiménez-Reyes, S. J., et al. 2007, Science, 316, 1591
Goodman, J. & Weare, J. 2010, Communications in Applied Mathematics and Computational Science, 5, 65
Grundahl, F., Kjeldsen, H., Christensen-Dalsgaard, J., Arentoft, T., & Frandsen, S. 2007, Communications in Asteroseismology, 150, 300
Harris, C. R., Millman, K. J., van der Walt, S. J., et al. 2020, Nature, 585, 357–362
Harvey, J. 1985, in ESA Special Publication, Vol. 235, Future Missions in Solar, Heliospheric & Space Plasma Physics, ed. E. Rolfe & B. Battrick, 199
Harvey, J. W., Hill, F., Hubbard, R. P., et al. 1996, Science, 272, 1284
Hill, H. A. & Stebbins, R. T. 1975, in Seventh Texas Symposium on Relativistic Astrophysics, ed. P. G. Bergman, E. J. Fenyves, & L. Motz, Vol. 262, 472–480
Howell, S. B., Sobeck, C., Haas, M., et al. 2014, PASP, 126, 398
Hunter, J. D. 2007, Computing in Science Engineering, 9, 90
Jiménez-Reyes, S. J., Chaplin, W. J., Elsworth, Y., et al. 2007, ApJ, 654, 1135
Kass, R. E. & Raftery, A. E. 1995, Journal of the American Statistical Association, 90, 773
Leibacher, J. W. & Stein, R. F. 1971, Astrophys. Lett., 7, 191
Leighton, R. B., Noyes, R. W., & Simon, G. W. 1962, ApJ, 135, 474
Liu, J. 2009, Monte Carlo Strategies in Scientic Computing
Mathis, S. 2013, Transport Processes in Stellar Interiors, ed. M. Goupil, K. Belkacem, C. Neiner, F. Lignières, & J. J. Green, Vol. 865, 23
Matthews, J. M., Kuschnig, R., Walker, G. A. H., et al. 2000, in Astronomical Society of the Pacific Conference Series, Vol. 203, IAU Colloq. 176: The Impact of Large-Scale Surveys on Pulsating Star Research, ed. L. Szabados & D. Kurtz, 74–75
Mosser, B., Barban, C., Montalbán, J., et al. 2011, A&A, 532, A86
Noyes, R. W. & Leighton, R. B. 1963, ApJ, 138, 631
Oliphant, T. 2006, NumPy: A guide to NumPy, USA: Trelgol Publishing
Pallé, P. L., Grundahl, F., Triviño Hage, A., et al. 2013, in Journal of Physics Conference Series, Vol. 440, Journal of Physics Conference Series, 012051
Palle, P. L., Regulo, C., & Roca Cortes, T. 1989, A&A, 224, 253
pandas development team, T. 2020, pandas-dev/pandas: Pandas
Ricker, G. R., Winn, J. N., Vanderspek, R., et al. 2015, Journal of Astronomical Telescopes, Instruments, and Systems, 1, 014003
Salabert, D., Fossat, E., Gelly, B., et al. 2004, A&A, 413, 1135
Salabert, D., Fossat, E., Gelly, B., et al. 2002, A&A, 390, 717
Salabert, D., Jiménez-Reyes, S. J., & Tomczyk, S. 2003, A&A, 408, 729
Salabert, D., Turck-Chièze, S., Barrière, J. C., et al. 2009, in Astronomical Society of the Pacific Conference Series, Vol. 416, Solar-Stellar Dynamos as Revealed by Helio- and Asteroseismology: GONG 2008/SOHO 21, ed. M. Dikpati, T. Arentoft, I. González Hernández, C. Lindsey, & F. Hill, 341
Scherrer, P. H. & Gough, D. O. 2019, ApJ, 877, 42
Schunker, H., Schou, J., Gaulme, P., & Gizon, L. 2018, Sol. Phys., 293, 95
Severnyi, A. B., Kotov, V. A., & Tsap, T. T. 1976, Nature, 259, 87
Sokal, A. 1997, Monte Carlo Methods in Statistical Mechanics: Foundations and New Algorithms, ed. C. DeWitt-Morette, P. Cartier, & A. Folacci (Boston, MA: Springer US), 131–192
Turck-Chièze, S., García, R. A., Couvidat, S., et al. 2004, ApJ, 604, 455
Turck-Chièze, S., Mathur, S., Ballot, J., et al. 2008, in Journal of Physics Conference Series, Vol. 118, Journal of Physics Conference Series, 012044
Ulrich, R. K. 1970, ApJ, 162, 993
Van Rossum, G. & Drake, F. L. 2009, Python 3 Reference Manual (Scotts Valley, CA: CreateSpace)
Vieu, T., Martínez González, M. J., Pastor Yabar, A., & Asensio Ramos, A. 2017, MNRAS, 465, 4414
Virtanen, P., Gommers, R., Oliphant, T. E., et al. 2020, Nature Methods, 17, 261
Wes McKinney. 2010, in Proceedings of the 9th Python in Science Conference, ed. Stéfan van der Walt & Jarrod Millman, 56 – 61
Woodard, M. F. 1984, PhD thesis, University of California, San Diego.
Woodard, M. F. & Noyes, R. W. 1985, Nature, 318, 449

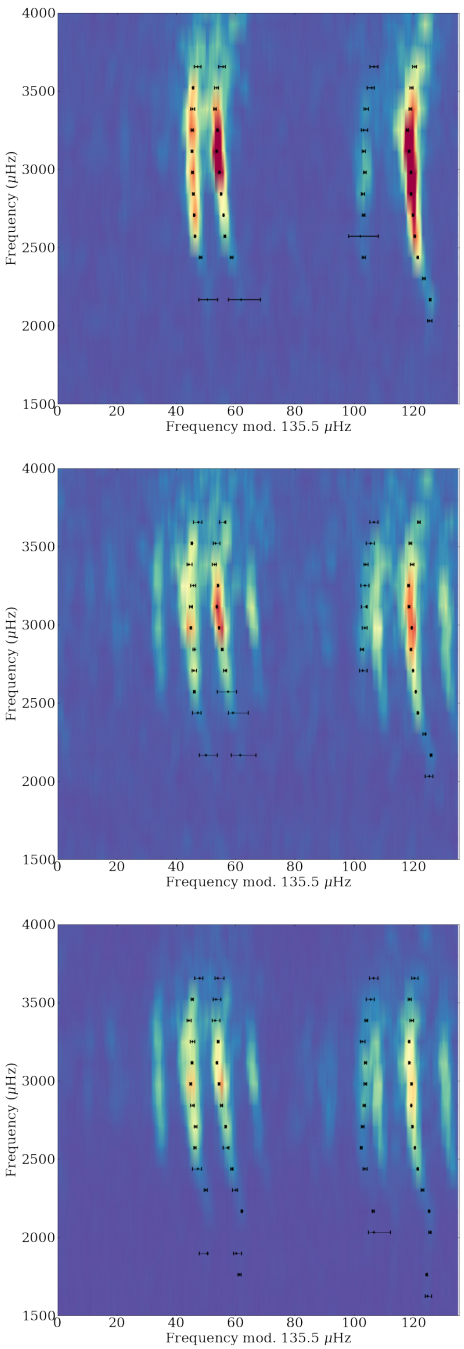

Fig. 9. Échelle diagram for GOLF (*top*), GOLF with Solar-SONG-like observational window (*middle*) and Solar-SONG (*bottom*). Fitted modes frequencies are represented in black.

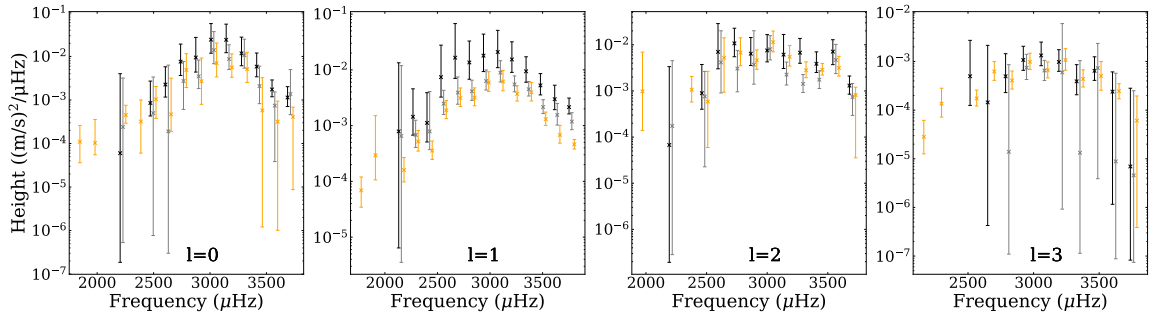

Fig. 10. Heights of the fitted modes for GOLF (black), GOLF with a Solar-SONG-like window (grey) and Solar-SONG (orange) spectra. The horizontal position of the markers has been slightly shifted for visualisation convenience.

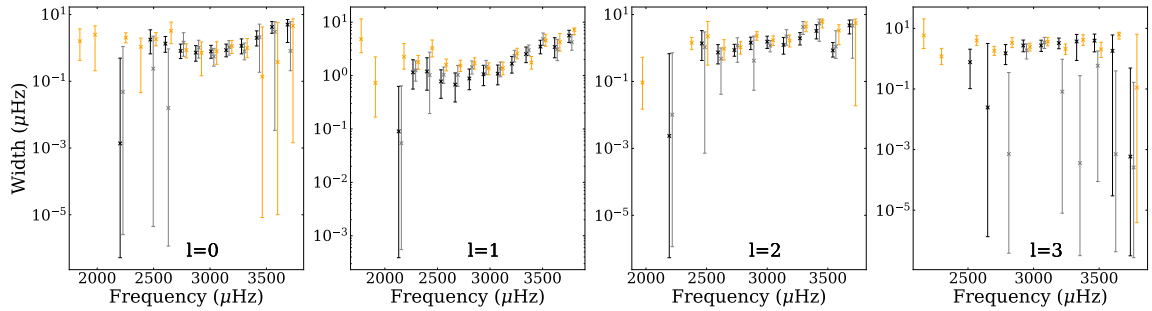

Fig. 11. Same as in Fig. 10 but for mode widths.

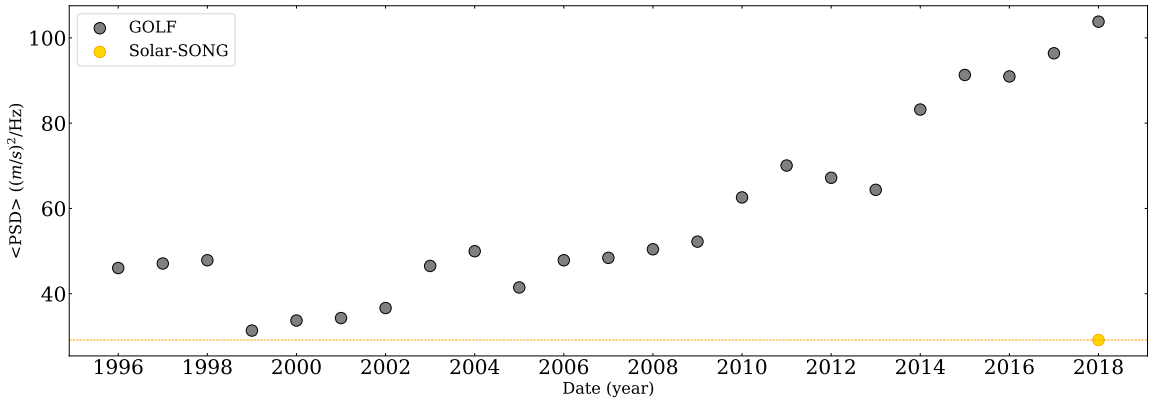

Fig. 12. Mean power in the 1 to 1.5 mHz region of the 30-day considered GOLF series spectra and for the Solar-SONG spectrum.

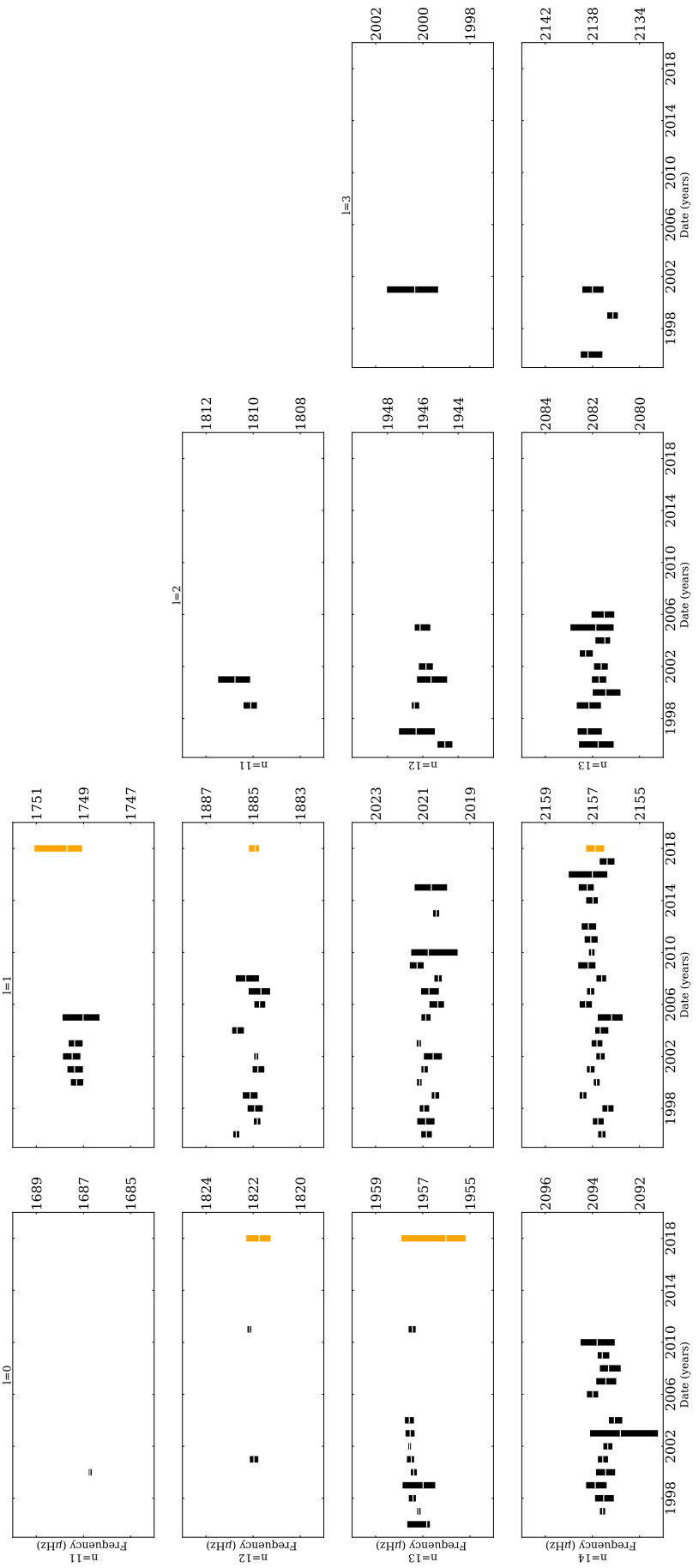

Fig. 13. Fitted mode frequencies and uncertainties for yearly GOLF 30-day series (black). The uncertainties on mode frequencies fitted within Solar-SONG spectrum are represented in orange for comparison purpose. The white tick signals the median value of the fitted distribution. For both instruments, only modes with an uncertainty below 2 μHz have been represented.

Appendix A: Fitting results for GOLF and Solar-SONG

The full summary of the GOLF and Solar-SONG fits performed for this work is presented in this section. Table A.1 presents the mode parameters obtained with GOLF, Table A.2 the mode parameters obtained with GOLF when applying a Solar-SONG-like window and Table A.3 the mode parameters obtained with Solar-SONG.

Appendix B: Solar-SONG data reduction module

The reduction process described in Sect. 2 can be performed with `songlib` submodule of `apollinaire`. The `standard_correction` function has been designed to process the `iSONG` cube outputs. The default settings of the function arguments are the ones that have been used to obtain the data used in this paper.

Table A.1. Parameters of the modes fitted in the GOLF spectrum.

n	l	ν (μHz)	H ($m^2 s^{-2} \mu Hz^{-1}$)	Γ (μHz)	$\ln K$
14	1	$2156.56^{+1.01}_{-0.61}$	$7.87 \times 10^{-4}\ ^{+1.26\times10^{-2}}_{-7.80\times10^{-4}}$	$0.09^{+0.54}_{-0.09}$	5.46
14	2	$2217.25^{+3.47}_{-2.94}$	$6.75 \times 10^{-5}\ ^{+3.29\times10^{-3}}_{-6.73\times10^{-5}}$	$0.002^{+0.68}_{-0.002}$	0.26
15	0	$2228.57^{+6.54}_{-4.21}$	$6.00 \times 10^{-5}\ ^{+3.96\times10^{-3}}_{-5.98\times10^{-5}}$	$0.001^{+0.49}_{-0.001}$	> 6
15	1	$2292.30^{+0.34}_{-0.32}$	$1.44 \times 10^{-3}\ ^{+3.13\times10^{-3}}_{-7.66\times10^{-4}}$	$1.15^{+0.83}_{-0.59}$	> 6
16	1	$2425.61^{+0.40}_{-0.42}$	$1.12 \times 10^{-3}\ ^{+2.78\times10^{-3}}_{-6.10\times10^{-4}}$	$1.19^{+0.96}_{-0.66}$	> 6
16	2	$2485.79^{+0.36}_{-0.44}$	$8.96 \times 10^{-4}\ ^{+2.85\times10^{-3}}_{-4.94\times10^{-4}}$	$1.37^{+1.94}_{-0.95}$	2.69
17	0	$2496.23^{+0.39}_{-0.49}$	$8.52 \times 10^{-4}\ ^{+1.86\times10^{-3}}_{-4.24\times10^{-4}}$	$1.78^{+1.71}_{-1.11}$	> 6
16	3	$2540.76^{+0.54}_{-0.55}$	$4.98 \times 10^{-4}\ ^{+2.23\times10^{-3}}_{-3.73\times10^{-4}}$	$0.77^{+1.29}_{-0.66}$	> 6
17	1	$2558.96^{+0.22}_{-0.20}$	$7.41 \times 10^{-3}\ ^{+2.03\times10^{-2}}_{-4.16\times10^{-3}}$	$0.78^{+0.50}_{-0.40}$	> 6
17	2	$2619.30^{+0.21}_{-0.22}$	$7.01 \times 10^{-3}\ ^{+2.18\times10^{-2}}_{-4.00\times10^{-3}}$	$0.74^{+0.53}_{-0.40}$	3.45
18	0	$2629.42^{+0.33}_{-0.33}$	$2.26 \times 10^{-3}\ ^{+3.52\times10^{-3}}_{-1.10\times10^{-3}}$	$1.34^{+0.86}_{-0.60}$	> 6
17	3	$2675.06^{+6.00}_{-3.94}$	$1.44 \times 10^{-4}\ ^{+2.01\times10^{-3}}_{-1.44\times10^{-4}}$	$0.02^{+3.14}_{-0.02}$	> 6
18	1	$2693.39^{+0.18}_{-0.20}$	$1.65 \times 10^{-2}\ ^{+5.11\times10^{-2}}_{-9.51\times10^{-3}}$	$0.68^{+0.44}_{-0.36}$	> 6
18	2	$2754.44^{+0.20}_{-0.20}$	$1.07 \times 10^{-2}\ ^{+1.21\times10^{-2}}_{-5.23\times10^{-3}}$	$0.87^{+0.42}_{-0.30}$	> 6
19	0	$2764.35^{+0.20}_{-0.21}$	$7.60 \times 10^{-3}\ ^{+1.16\times10^{-2}}_{-3.94\times10^{-3}}$	$0.82^{+0.49}_{-0.34}$	> 6
18	3	$2811.52^{+0.47}_{-0.47}$	$4.97 \times 10^{-4}\ ^{+9.50\times10^{-4}}_{-2.67\times10^{-4}}$	$1.51^{+1.41}_{-0.87}$	> 6
19	1	$2828.19^{+0.20}_{-0.19}$	$1.36 \times 10^{-2}\ ^{+1.93\times10^{-2}}_{-6.79\times10^{-3}}$	$0.88^{+0.45}_{-0.34}$	> 6
19	2	$2889.57^{+0.27}_{-0.26}$	$6.41 \times 10^{-3}\ ^{+7.97\times10^{-3}}_{-2.85\times10^{-3}}$	$1.45^{+0.66}_{-0.55}$	> 6
20	0	$2898.94^{+0.19}_{-0.20}$	$9.46 \times 10^{-3}\ ^{+1.79\times10^{-2}}_{-5.09\times10^{-3}}$	$0.72^{+0.45}_{-0.32}$	> 6
19	3	$2946.68^{+0.52}_{-0.48}$	$1.08 \times 10^{-3}\ ^{+9.82\times10^{-4}}_{-4.17\times10^{-4}}$	$2.72^{+1.40}_{-1.02}$	> 6
20	1	$2963.01^{+0.21}_{-0.22}$	$1.80 \times 10^{-2}\ ^{+2.58\times10^{-2}}_{-8.65\times10^{-3}}$	$1.06^{+0.50}_{-0.41}$	> 6
20	2	$3024.69^{+0.30}_{-0.28}$	$7.55 \times 10^{-3}\ ^{+9.10\times10^{-3}}_{-3.28\times10^{-3}}$	$1.55^{+0.71}_{-0.58}$	> 6
21	0	$3033.76^{+0.18}_{-0.19}$	$2.43 \times 10^{-2}\ ^{+3.26\times10^{-2}}_{-1.24\times10^{-2}}$	$0.78^{+0.41}_{-0.29}$	> 6
20	3	$3082.84^{+0.45}_{-0.46}$	$1.33 \times 10^{-3}\ ^{+1.18\times10^{-3}}_{-5.11\times10^{-4}}$	$2.74^{+1.34}_{-1.00}$	> 6
21	1	$3098.37^{+0.21}_{-0.22}$	$2.09 \times 10^{-2}\ ^{+3.02\times10^{-2}}_{-9.96\times10^{-3}}$	$1.09^{+0.49}_{-0.42}$	> 6
21	2	$3160.00^{+0.31}_{-0.29}$	$6.12 \times 10^{-3}\ ^{+1.06\times10^{-2}}_{-3.05\times10^{-3}}$	$1.24^{+0.83}_{-0.58}$	> 6
22	0	$3168.26^{+0.19}_{-0.20}$	$2.41 \times 10^{-2}\ ^{+3.11\times10^{-2}}_{-1.19\times10^{-2}}$	$0.86^{+0.44}_{-0.32}$	> 6
21	3	$3217.81^{+0.57}_{-0.55}$	$9.81 \times 10^{-4}\ ^{+7.69\times10^{-4}}_{-3.53\times10^{-4}}$	$3.28^{+1.50}_{-1.16}$	> 6
22	1	$3233.12^{+0.26}_{-0.26}$	$1.54 \times 10^{-2}\ ^{+1.65\times10^{-2}}_{-6.34\times10^{-3}}$	$1.67^{+0.62}_{-0.56}$	> 6
22	2	$3295.47^{+0.37}_{-0.34}$	$6.73 \times 10^{-3}\ ^{+6.99\times10^{-3}}_{-2.76\times10^{-3}}$	$1.95^{+0.92}_{-0.72}$	5.41
23	0	$3304.00^{+0.25}_{-0.25}$	$1.18 \times 10^{-2}\ ^{+1.60\times10^{-2}}_{-5.67\times10^{-3}}$	$1.15^{+0.71}_{-0.49}$	> 6
22	3	$3353.27^{+1.24}_{-0.80}$	$3.91 \times 10^{-4}\ ^{+4.70\times10^{-4}}_{-1.84\times10^{-4}}$	$3.70^{+2.63}_{-2.82}$	> 6
23	1	$3367.99^{+0.34}_{-0.36}$	$9.42 \times 10^{-3}\ ^{+7.74\times10^{-3}}_{-3.43\times10^{-3}}$	$2.53^{+0.90}_{-0.78}$	> 6
23	2	$3430.96^{+0.75}_{-0.60}$	$3.87 \times 10^{-3}\ ^{+3.15\times10^{-3}}_{-1.35\times10^{-3}}$	$3.24^{+1.72}_{-1.38}$	0.26
24	0	$3438.61^{+0.41}_{-0.56}$	$5.84 \times 10^{-3}\ ^{+6.14\times10^{-3}}_{-2.43\times10^{-3}}$	$2.01^{+1.24}_{-0.86}$	0.26
23	3	$3489.45^{+0.89}_{-0.68}$	$6.45 \times 10^{-4}\ ^{+6.05\times10^{-4}}_{-2.35\times10^{-4}}$	$3.94^{+2.55}_{-2.26}$	> 6
24	1	$3504.45^{+0.44}_{-0.45}$	$5.27 \times 10^{-3}\ ^{+3.30\times10^{-3}}_{-1.71\times10^{-3}}$	$3.49^{+1.09}_{-0.93}$	> 6
24	2	$3566.53^{+0.24}_{-0.21}$	$7.12 \times 10^{-3}\ ^{+5.77\times10^{-3}}_{-3.40\times10^{-3}}$	$0.85^{+0.62}_{-0.31}$	2.69
25	0	$3574.54^{+0.69}_{-0.73}$	$1.74 \times 10^{-3}\ ^{+1.14\times10^{-3}}_{-5.58\times10^{-4}}$	$4.25^{+1.91}_{-1.51}$	2.69
24	3	$3626.70^{+1.06}_{-1.51}$	$2.40 \times 10^{-4}\ ^{+3.72\times10^{-4}}_{-2.39\times10^{-4}}$	$1.81^{+4.25}_{-1.81}$	> 6
25	1	$3640.23^{+0.49}_{-0.50}$	$2.98 \times 10^{-3}\ ^{+2.33\times10^{-3}}_{-1.04\times10^{-3}}$	$3.42^{+1.70}_{-1.27}$	> 6
25	2	$3703.51^{+1.18}_{-1.08}$	$1.30 \times 10^{-3}\ ^{+8.03\times10^{-4}}_{-4.52\times10^{-4}}$	$4.76^{+2.09}_{-2.12}$	-0.10
26	0	$3712.14^{+0.72}_{-1.57}$	$1.14 \times 10^{-3}\ ^{+8.84\times10^{-4}}_{-4.32\times10^{-4}}$	$4.99^{+2.12}_{-3.54}$	0.41
25	3	$3762.94^{+1.39}_{-1.34}$	$6.95 \times 10^{-6}\ ^{+2.76\times10^{-4}}_{-6.87\times10^{-6}}$	$0.00^{+0.49}_{-0.00}$	1.54
26	1	$3776.70^{+0.64}_{-0.67}$	$2.15 \times 10^{-3}\ ^{+9.73\times10^{-4}}_{-5.27\times10^{-4}}$	$5.63^{+1.41}_{-1.47}$	4.01

Table A.2. Same as Table A.1 but for the GOLF spectrum obtained with the series multiplied by the Solar-SONG-like window.

n	l	ν (μHz)	H ($m^2s^{-2}\mu Hz^{-1}$)	Γ (μHz)	$\ln K$
14	1	$2156.62^{+1.21}_{-1.30}$	6.52×10^{-4} $^{+1.13\times10^{-2}}_{-6.48\times10^{-4}}$	$0.05^{+0.59}_{-0.05}$	5.46
14	2	$2216.78^{+3.75}_{-2.24}$	1.74×10^{-4} $^{+4.36\times10^{-3}}_{-1.74\times10^{-4}}$	$0.01^{+0.71}_{-0.01}$	0.26
15	0	$2228.28^{+5.29}_{-3.07}$	2.40×10^{-4} $^{+2.95\times10^{-3}}_{-2.39\times10^{-4}}$	$0.05^{+1.05}_{-0.05}$	> 6
15	1	$2292.62^{+0.30}_{-0.33}$	6.82×10^{-4} $^{+5.67\times10^{-4}}_{-2.75\times10^{-4}}$	$1.25^{+0.64}_{-0.47}$	> 6
16	1	$2426.08^{+0.19}_{-0.69}$	7.87×10^{-4} $^{+3.31\times10^{-3}}_{-4.16\times10^{-4}}$	$1.02^{+1.72}_{-0.83}$	> 6
16	2	$2484.91^{+1.01}_{-1.84}$	7.60×10^{-4} $^{+1.89\times10^{-3}}_{-7.38\times10^{-4}}$	$1.06^{+1.96}_{-1.06}$	2.69
17	0	$2496.71^{+5.07}_{-1.54}$	4.98×10^{-4} $^{+2.87\times10^{-3}}_{-4.98\times10^{-4}}$	$0.24^{+2.01}_{-0.24}$	> 6
17	1	$2558.99^{+0.18}_{-0.18}$	2.48×10^{-3} $^{+1.81\times10^{-3}}_{-8.91\times10^{-4}}$	$1.04^{+0.41}_{-0.32}$	> 6
17	2	$2619.03^{+0.29}_{-0.30}$	4.15×10^{-3} $^{+1.60\times10^{-2}}_{-3.25\times10^{-3}}$	$0.48^{+0.52}_{-0.44}$	3.45
18	0	$2630.51^{+2.80}_{-3.78}$	1.90×10^{-4} $^{+6.14\times10^{-3}}_{-1.89\times10^{-4}}$	$0.02^{+0.92}_{-0.02}$	> 6
18	1	$2693.69^{+0.16}_{-0.18}$	3.92×10^{-3} $^{+3.54\times10^{-3}}_{-1.50\times10^{-3}}$	$1.03^{+0.52}_{-0.40}$	> 6
18	2	$2754.27^{+0.91}_{-0.55}$	3.05×10^{-3} $^{+4.50\times10^{-3}}_{-2.09\times10^{-3}}$	$1.18^{+0.83}_{-0.81}$	> 6
19	0	$2764.99^{+0.48}_{-0.71}$	2.72×10^{-3} $^{+4.92\times10^{-3}}_{-2.12\times10^{-3}}$	$1.44^{+1.41}_{-0.88}$	> 6
18	3	$2811.30^{+1.43}_{-1.16}$	1.39×10^{-5} $^{+8.48\times10^{-4}}_{-1.38\times10^{-5}}$	$0.00^{+0.35}_{-0.00}$	> 6
19	1	$2828.25^{+0.20}_{-0.19}$	4.13×10^{-3} $^{+2.40\times10^{-3}}_{-1.29\times10^{-3}}$	$1.44^{+0.44}_{-0.37}$	> 6
19	2	$2889.99^{+0.11}_{-0.56}$	3.71×10^{-3} $^{+1.64\times10^{-2}}_{-2.31\times10^{-3}}$	$0.42^{+1.86}_{-0.36}$	> 6
20	0	$2899.28^{+0.31}_{-0.27}$	3.49×10^{-3} $^{+4.76\times10^{-3}}_{-1.66\times10^{-3}}$	$1.02^{+0.68}_{-0.52}$	> 6
19	3	$2946.46^{+0.54}_{-0.52}$	7.48×10^{-4} $^{+6.60\times10^{-4}}_{-3.22\times10^{-4}}$	$1.88^{+1.19}_{-0.90}$	> 6
20	1	$2962.95^{+0.18}_{-0.18}$	6.30×10^{-3} $^{+3.65\times10^{-3}}_{-1.95\times10^{-3}}$	$1.46^{+0.46}_{-0.41}$	> 6
20	2	$3024.14^{+0.25}_{-0.26}$	8.03×10^{-3} $^{+7.75\times10^{-3}}_{-3.33\times10^{-3}}$	$1.18^{+0.49}_{-0.41}$	> 6
21	0	$3033.66^{+0.20}_{-0.18}$	1.40×10^{-2} $^{+2.32\times10^{-2}}_{-7.16\times10^{-3}}$	$0.56^{+0.42}_{-0.27}$	> 6
20	3	$3082.76^{+0.81}_{-0.80}$	6.52×10^{-4} $^{+4.04\times10^{-4}}_{-2.46\times10^{-4}}$	$3.43^{+1.62}_{-1.26}$	> 6
21	1	$3098.64^{+0.17}_{-0.18}$	8.91×10^{-3} $^{+5.67\times10^{-3}}_{-2.86\times10^{-3}}$	$1.34^{+0.45}_{-0.40}$	> 6
21	2	$3159.64^{+0.49}_{-0.53}$	2.26×10^{-3} $^{+1.96\times10^{-3}}_{-9.12\times10^{-4}}$	$2.22^{+1.31}_{-1.00}$	> 6
22	0	$3168.30^{+0.23}_{-0.22}$	8.72×10^{-3} $^{+9.79\times10^{-3}}_{-3.70\times10^{-3}}$	$1.05^{+0.60}_{-0.44}$	> 6
21	3	$3218.70^{+0.30}_{-1.66}$	5.99×10^{-4} $^{+5.43\times10^{-3}}_{-5.98\times10^{-4}}$	$0.08^{+0.88}_{-0.08}$	> 6
22	1	$3233.12^{+0.27}_{-0.28}$	5.49×10^{-3} $^{+2.30\times10^{-3}}_{-1.44\times10^{-3}}$	$2.34^{+0.63}_{-0.54}$	> 6
22	2	$3295.79^{+0.81}_{-0.92}$	1.43×10^{-3} $^{+8.41\times10^{-4}}_{-4.98\times10^{-4}}$	$4.24^{+1.94}_{-1.70}$	5.41
23	0	$3304.16^{+0.19}_{-0.22}$	1.07×10^{-2} $^{+1.43\times10^{-2}}_{-5.30\times10^{-3}}$	$0.79^{+0.61}_{-0.35}$	> 6
22	3	$3353.68^{+1.34}_{-1.37}$	1.33×10^{-5} $^{+1.03\times10^{-3}}_{-1.32\times10^{-5}}$	$0.00^{+0.27}_{-0.00}$	> 6
23	1	$3368.36^{+0.28}_{-0.29}$	4.49×10^{-3} $^{+1.68\times10^{-3}}_{-1.10\times10^{-3}}$	$3.01^{+0.73}_{-0.65}$	> 6
23	2	$3429.81^{+0.95}_{-0.63}$	1.75×10^{-3} $^{+9.79\times10^{-4}}_{-6.27\times10^{-4}}$	$5.42^{+1.85}_{-3.83}$	0.26
24	0	$3438.40^{+0.52}_{-0.79}$	2.08×10^{-3} $^{+3.89\times10^{-3}}_{-1.26\times10^{-3}}$	$2.10^{+3.06}_{-1.91}$	0.26
23	3	$3489.34^{+0.79}_{-0.57}$	7.33×10^{-4} $^{+1.62\times10^{-3}}_{-7.29\times10^{-4}}$	$0.59^{+1.21}_{-0.59}$	> 6
24	1	$3504.99^{+0.58}_{-0.64}$	2.15×10^{-3} $^{+7.67\times10^{-4}}_{-5.08\times10^{-4}}$	$4.84^{+1.43}_{-1.15}$	> 6
24	2	$3566.21^{+0.21}_{-0.31}$	4.69×10^{-3} $^{+5.50\times10^{-3}}_{-2.32\times10^{-3}}$	$1.11^{+2.18}_{-0.62}$	2.69
25	0	$3574.11^{+1.44}_{-0.83}$	7.41×10^{-4} $^{+7.89\times10^{-4}}_{-7.02\times10^{-4}}$	$3.06^{+3.03}_{-3.05}$	2.69
24	3	$3626.40^{+1.30}_{-1.43}$	8.83×10^{-6} $^{+5.66\times10^{-4}}_{-8.75\times10^{-6}}$	$0.00^{+0.39}_{-0.00}$	> 6
25	1	$3639.76^{+0.52}_{-0.42}$	1.55×10^{-3} $^{+9.49\times10^{-4}}_{-5.27\times10^{-4}}$	$3.11^{+1.67}_{-1.21}$	> 6
25	2	$3703.81^{+1.19}_{-1.75}$	7.37×10^{-4} $^{+7.15\times10^{-4}}_{-4.43\times10^{-4}}$	$4.63^{+2.32}_{-4.13}$	-0.10
26	0	$3712.76^{+0.23}_{-1.89}$	1.37×10^{-3} $^{+3.63\times10^{-3}}_{-9.10\times10^{-4}}$	$0.82^{+5.29}_{-0.61}$	0.41
25	3	$3762.95^{+1.38}_{-1.34}$	4.57×10^{-6} $^{+2.46\times10^{-4}}_{-4.49\times10^{-6}}$	$0.00^{+0.17}_{-0.00}$	1.54
26	1	$3778.16^{+0.43}_{-0.54}$	1.18×10^{-3} $^{+5.23\times10^{-4}}_{-3.34\times10^{-4}}$	$4.20^{+1.62}_{-1.22}$	4.01

Table A.3. Same as Table A.1, but for Solar-SONG spectrum.

n	l	ν (μHz)	H ($m^2 s^{-2} \mu Hz^{-1}$)	Γ (μHz)	$\ln K$
11	1	$1749.70^{+1.38}_{-0.64}$	6.90×10^{-5} $^{+5.08\times10^{-5}}_{-3.46\times10^{-5}}$	$4.82^{+6.68}_{-2.14}$	> 6
12	0	$1821.74^{+0.55}_{-0.48}$	1.10×10^{-4} $^{+1.50\times10^{-4}}_{-7.37\times10^{-5}}$	$1.59^{+2.11}_{-1.17}$	2.84
12	1	$1884.92^{+0.26}_{-0.16}$	2.94×10^{-4} $^{+1.22\times10^{-3}}_{-1.88\times10^{-4}}$	$0.73^{+1.51}_{-0.56}$	5.09
12	2	$1946.35^{+0.12}_{-2.68}$	9.81×10^{-4} $^{+5.96\times10^{-3}}_{-8.42\times10^{-4}}$	$0.09^{+0.44}_{-0.08}$	2.46
13	0	$1956.02^{+1.89}_{-0.83}$	1.03×10^{-4} $^{+2.51\times10^{-4}}_{-4.83\times10^{-5}}$	$2.50^{+2.09}_{-2.29}$	5.97
13	3	$2137.99^{+5.50}_{-1.80}$	2.83×10^{-5} $^{+3.35\times10^{-5}}_{-1.57\times10^{-5}}$	$5.83^{+14.65}_{-3.66}$	3.85
14	1	$2156.88^{+0.39}_{-0.37}$	1.60×10^{-4} $^{+1.08\times10^{-4}}_{-6.22\times10^{-5}}$	$2.25^{+1.73}_{-0.93}$	5.46
15	0	$2228.84^{+0.28}_{-0.28}$	4.51×10^{-4} $^{+3.04\times10^{-4}}_{-1.58\times10^{-4}}$	$2.04^{+0.80}_{-0.62}$	> 6
14	3	$2273.12^{+0.33}_{-0.35}$	1.36×10^{-4} $^{+1.47\times10^{-4}}_{-6.39\times10^{-5}}$	$1.19^{+1.00}_{-0.55}$	> 6
15	1	$2291.96^{+0.22}_{-0.22}$	5.20×10^{-4} $^{+2.96\times10^{-4}}_{-1.70\times10^{-4}}$	$1.78^{+0.60}_{-0.48}$	> 6
15	2	$2352.09^{+0.51}_{-0.56}$	1.06×10^{-3} $^{+9.99\times10^{-4}}_{-4.85\times10^{-4}}$	$1.44^{+0.63}_{-0.55}$	> 6
16	0	$2362.11^{+0.65}_{-0.98}$	3.20×10^{-4} $^{+6.79\times10^{-4}}_{-2.60\times10^{-4}}$	$1.08^{+0.89}_{-1.04}$	> 6
16	1	$2425.13^{+0.42}_{-0.45}$	3.56×10^{-4} $^{+1.73\times10^{-4}}_{-1.09\times10^{-4}}$	$3.28^{+1.35}_{-1.05}$	> 6
16	2	$2484.81^{+1.25}_{-1.83}$	5.88×10^{-4} $^{+2.07\times10^{-3}}_{-5.28\times10^{-4}}$	$2.24^{+3.97}_{-1.93}$	2.69
17	0	$2496.32^{+0.37}_{-0.44}$	1.04×10^{-3} $^{+9.98\times10^{-4}}_{-6.63\times10^{-4}}$	$1.83^{+1.04}_{-0.68}$	> 6
16	3	$2541.18^{+0.69}_{-0.61}$	1.74×10^{-4} $^{+8.41\times10^{-5}}_{-5.28\times10^{-5}}$	$3.99^{+1.74}_{-1.24}$	> 6
17	1	$2558.99^{+0.18}_{-0.18}$	1.88×10^{-3} $^{+9.33\times10^{-4}}_{-5.44\times10^{-4}}$	$1.60^{+0.44}_{-0.37}$	> 6
17	2	$2619.22^{+0.42}_{-0.29}$	5.23×10^{-3} $^{+8.91\times10^{-3}}_{-4.29\times10^{-3}}$	$0.95^{+0.82}_{-0.51}$	3.45
18	0	$2630.22^{+0.57}_{-1.48}$	4.67×10^{-4} $^{+2.70\times10^{-3}}_{-2.77\times10^{-4}}$	$3.25^{+2.71}_{-1.91}$	> 6
17	3	$2675.37^{+0.29}_{-0.26}$	6.23×10^{-4} $^{+3.76\times10^{-4}}_{-2.12\times10^{-4}}$	$1.84^{+0.72}_{-0.55}$	> 6
18	1	$2693.40^{+0.17}_{-0.17}$	3.12×10^{-3} $^{+1.61\times10^{-3}}_{-9.15\times10^{-4}}$	$1.54^{+0.40}_{-0.35}$	> 6
18	2	$2754.96^{+0.38}_{-0.56}$	6.75×10^{-3} $^{+7.39\times10^{-3}}_{-3.24\times10^{-3}}$	$1.05^{+0.49}_{-0.39}$	> 6
19	0	$2765.04^{+0.24}_{-0.30}$	4.89×10^{-3} $^{+6.68\times10^{-3}}_{-2.96\times10^{-3}}$	$0.86^{+0.47}_{-0.35}$	> 6
18	3	$2811.24^{+0.46}_{-0.48}$	4.08×10^{-4} $^{+2.29\times10^{-4}}_{-1.37\times10^{-4}}$	$3.36^{+1.56}_{-1.04}$	> 6
19	1	$2828.02^{+0.19}_{-0.19}$	3.19×10^{-3} $^{+1.56\times10^{-3}}_{-9.14\times10^{-4}}$	$1.71^{+0.44}_{-0.38}$	> 6
19	2	$2889.39^{+0.48}_{-0.65}$	4.61×10^{-3} $^{+3.11\times10^{-3}}_{-1.66\times10^{-3}}$	$2.34^{+0.73}_{-0.63}$	> 6
20	0	$2899.11^{+0.34}_{-0.35}$	2.70×10^{-3} $^{+6.48\times10^{-3}}_{-1.91\times10^{-3}}$	$0.71^{+0.79}_{-0.57}$	> 6
19	3	$2947.19^{+0.36}_{-0.34}$	9.86×10^{-4} $^{+4.95\times10^{-4}}_{-2.97\times10^{-4}}$	$2.44^{+0.83}_{-0.64}$	> 6
20	1	$2963.07^{+0.16}_{-0.16}$	5.92×10^{-3} $^{+3.33\times10^{-3}}_{-1.83\times10^{-3}}$	$1.37^{+0.37}_{-0.33}$	> 6
20	2	$3024.12^{+0.30}_{-0.31}$	1.14×10^{-2} $^{+8.41\times10^{-3}}_{-4.38\times10^{-3}}$	$1.70^{+0.60}_{-0.51}$	> 6
21	0	$3033.63^{+0.34}_{-0.22}$	7.02×10^{-3} $^{+1.33\times10^{-2}}_{-3.63\times10^{-3}}$	$0.80^{+0.73}_{-0.47}$	> 6
20	3	$3082.99^{+0.51}_{-0.52}$	6.62×10^{-4} $^{+3.21\times10^{-4}}_{-2.01\times10^{-4}}$	$3.64^{+1.40}_{-0.98}$	> 6
21	1	$3098.54^{+0.16}_{-0.17}$	6.18×10^{-3} $^{+3.62\times10^{-3}}_{-1.96\times10^{-3}}$	$1.38^{+0.41}_{-0.35}$	> 6
21	2	$3159.98^{+0.30}_{-0.34}$	5.49×10^{-3} $^{+4.17\times10^{-3}}_{-2.03\times10^{-3}}$	$1.66^{+0.77}_{-0.59}$	> 6
22	0	$3168.33^{+0.25}_{-0.22}$	5.60×10^{-3} $^{+5.87\times10^{-3}}_{-2.28\times10^{-3}}$	$1.13^{+0.55}_{-0.45}$	> 6
21	3	$3218.43^{+0.36}_{-0.41}$	1.07×10^{-3} $^{+7.68\times10^{-4}}_{-4.07\times10^{-4}}$	$2.09^{+0.97}_{-0.70}$	> 6
22	1	$3233.19^{+0.27}_{-0.28}$	3.71×10^{-3} $^{+1.48\times10^{-3}}_{-9.45\times10^{-4}}$	$2.59^{+0.65}_{-0.54}$	> 6
22	2	$3295.56^{+0.72}_{-0.85}$	2.80×10^{-3} $^{+1.47\times10^{-3}}_{-8.61\times10^{-4}}$	$4.39^{+1.60}_{-1.33}$	5.41
23	0	$3304.19^{+0.27}_{-0.28}$	5.11×10^{-3} $^{+7.38\times10^{-3}}_{-2.59\times10^{-3}}$	$0.99^{+0.92}_{-0.48}$	> 6
22	3	$3352.78^{+0.81}_{-0.60}$	4.39×10^{-4} $^{+2.35\times10^{-4}}_{-1.39\times10^{-4}}$	$4.18^{+1.99}_{-1.41}$	> 6
23	1	$3368.58^{+0.20}_{-0.21}$	3.94×10^{-3} $^{+2.00\times10^{-3}}_{-1.18\times10^{-3}}$	$1.76^{+0.52}_{-0.43}$	> 6
23	2	$3429.70^{+0.75}_{-0.56}$	2.86×10^{-3} $^{+1.09\times10^{-3}}_{-6.49\times10^{-4}}$	$6.09^{+1.29}_{-2.10}$	0.26
24	0	$3438.58^{+1.57}_{-0.99}$	5.76×10^{-4} $^{+2.67\times10^{-3}}_{-5.75\times10^{-4}}$	$0.14^{+4.11}_{-0.14}$	0.26
23	3	$3489.57^{+0.45}_{-0.49}$	5.03×10^{-4} $^{+4.99\times10^{-4}}_{-2.46\times10^{-4}}$	$2.03^{+1.42}_{-0.93}$	> 6
24	1	$3504.93^{+0.55}_{-0.61}$	1.31×10^{-3} $^{+4.44\times10^{-4}}_{-2.98\times10^{-4}}$	$4.57^{+1.36}_{-1.03}$	> 6
24	2	$3566.33^{+0.37}_{-0.41}$	3.17×10^{-3} $^{+2.45\times10^{-3}}_{-1.07\times10^{-3}}$	$3.32^{+1.63}_{-2.06}$	2.69
25	0	$3574.31^{+1.64}_{-0.98}$	3.17×10^{-4} $^{+6.21\times10^{-4}}_{-3.16\times10^{-4}}$	$0.38^{+5.44}_{-0.38}$	2.69
24	3	$3626.45^{+1.20}_{-1.45}$	2.45×10^{-4} $^{+1.04\times10^{-4}}_{-7.44\times10^{-5}}$	$6.21^{+1.25}_{-1.77}$	> 6
25	1	$3639.53^{+0.55}_{-0.51}$	6.82×10^{-4} $^{+3.28\times10^{-4}}_{-1.97\times10^{-4}}$	$4.25^{+1.91}_{-1.38}$	> 6
25	2	$3704.25^{+0.94}_{-1.66}$	8.13×10^{-4} $^{+3.91\times10^{-4}}_{-7.77\times10^{-4}}$	$5.56^{+1.82}_{-5.54}$	-0.10
26	0	$3710.29^{+2.18}_{-0.94}$	4.10×10^{-4} $^{+2.73\times10^{-4}}_{-4.01\times10^{-4}}$	$4.57^{+2.81}_{-4.57}$	0.41
25	3	$3762.77^{+1.53}_{-1.30}$	6.09×10^{-5} $^{+1.35\times10^{-4}}_{-6.05\times10^{-5}}$	$0.11^{+6.28}_{-0.11}$	1.54
26	1	$3776.68^{+1.12}_{-1.04}$	4.62×10^{-4} $^{+9.98\times10^{-5}}_{-8.21\times10^{-5}}$	$7.14^{+0.64}_{-1.33}$	4.01